ACS APPLIED MATERIALS & INTERFACES

Research Article

www.acsami.org

New Insights into the Microstructure-Separation Properties of Organosilica Membranes with Ethane, Ethylene, and Acetylene Bridges

Rong Xu,[†] Suhaina M. Ibrahim,[‡] Masakoto Kanezashi,[‡] Tomohisa Yoshioka,[‡] Kenji Ito,[§] Joji Ohshita,[‡] and Toshinori Tsuru*[,‡]

[†]Jiangsu Key Laboratory of Advanced Catalytic Materials and Technology, School of Petrochemical Engineering, Changzhou University, Changzhou 213164, China

[‡]Department of Chemical Engineering, Hiroshima University, Higashi-Hiroshima 739-8527, Japan

[§]National Institute of Advanced Industrial Science and Technology (AIST), Tsukuba 305-8565, Japan

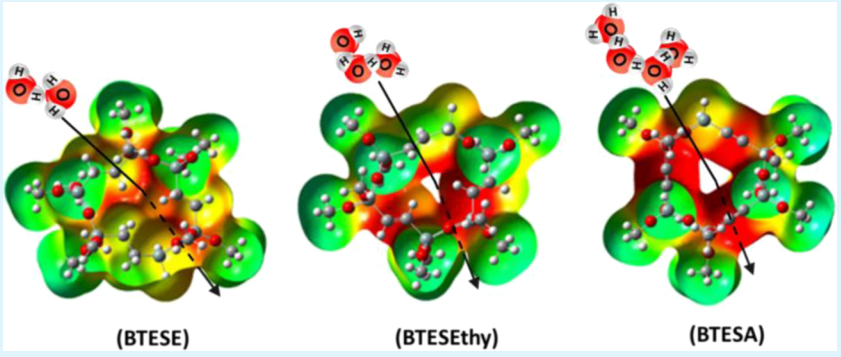

ABSTRACT: Microporous organosilica membranes with ethane, ethylene, and acetylene bridges have been developed and the extensive microstructural characterization has been discussed in relation with separation properties of the membrane. The organosilica network structure and the membrane performances can be controlled by adjusting the flexibility, size, and electronic structure of the bridging groups. A relatively narrow size distribution was obtained for the novel acetylene-bridged sol by optimizing the sol synthesis. Incorporation of larger rigid bridges into organosilica networks resulted in a looser microstructure of the membrane, which was quantitatively evaluated by N_2 sorption and positron annihilation lifetime (PAL) measurements. Molecular weight cutoff (MWCO) measurements indicated that the acetylene-bridged membrane had a larger effective separation pore size than ethane- and ethylene-bridged membranes, leading to a relatively low NaCl rejection in reverse osmosis. In quantum chemical calculations, a more open pore structure and increased polarization was observed for the acetylene-bridged networks, which led to a significant improvement in water permeability. The present study will offer new insight into design of high-performance molecular separation membranes.

KEYWORDS: *organosilica, membrane, microstructure, gas separation, reverse osmosis*

INTRODUCTION

Organically bridged silica materials have attracted much interest due to interesting features such as a high surface area, improved hydrothermal stability, and superior chemical resistance.[1,2] These materials, commonly known as periodic mesoporous organosilicas (PMOs), were synthesized via the hydrolysis and condensation of bridged organosilanes $(R'O)_3Si-R-Si-(OR')_3$.[3−5] The versatility of incorporated organic bridges (R) provides new opportunities to finely tune the chemical-physical properties, which makes PMOs highly promising for a wide range of applications.[6,7] However, the applicability of PMOs to molecular separation is severely limited by their pore size (typically ranging from ∼2 to 10 nm), which seems too large to exhibit molecular sieving ability. Generally, membranes with pore sizes of <1 nm are applied to the separation of small molecules through molecular sieving and/or affinity to guest molecules.

Castricum et al. first developed microporous organically bridged silica membranes by co-condensation of bis-(triethoxysilyl)ethane (BTESE) and methyltriethoxysilane. The resultant membranes, with a pore diameter of ∼0.4 nm, delivered a quite stable performance over 2 years for the pervaporative dehydration of butanol at 150 °C.[8,9] Our research group proposed a "spacer" technique to control silica networks, where ethane groups were introduced to design a looser structure for the development of a highly permeable hydrogen

Received: March 24, 2014
Accepted: May 29, 2014
Published: May 29, 2014

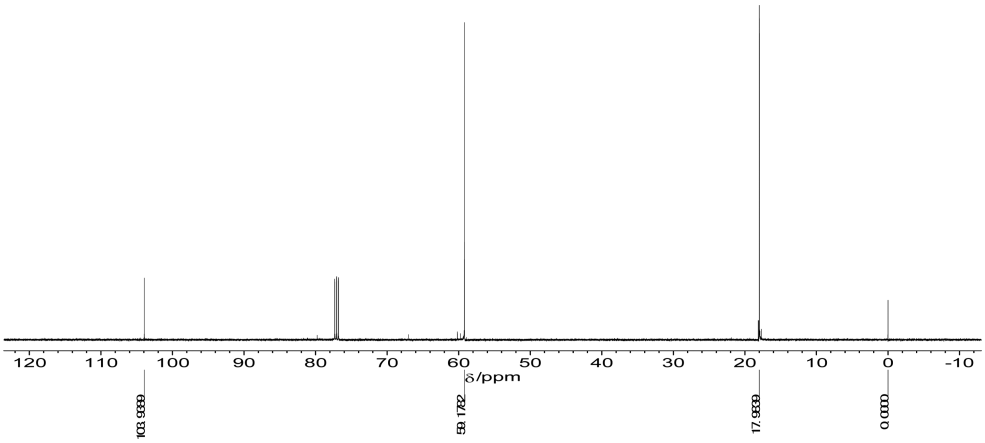

Figure 1. ^{13}C NMR spectra of BTESA in $CDCl_3$.

separation membrane.[10] Recently, the applications of organosilica membranes have expanded, for instance, to CO_2 separation and water desalination,[11−13] due to its excellent molecular sieving ability and exceptional hydrothermal stability.

To date, most work on organosilica membranes has focused on BTESE-derived materials since the ethane bridges (−CH_2−CH_2−) in the networks benefits the formation of small and rigid pores for molecular sieving. From this point of view, the development of organosilica membranes with unsaturated ethylene or acetylene bridges deserves a greater amount of interest, because these materials are easily accessible for chemical modification while maintaining a rigid pore structure. Recently, we successfully explored ethylene-bridged (−CH═CH−) organosilica membranes with improved permeability for water desalination,[14] and in the present study we present further developments of acetylene-bridged (−C≡C−) microporous organosilica membranes using a novel precursor, bis(triethoxysilyl)acetylene (BTESA). The introduction of more polarizable and rigid acetylene bridges would make organosilica networks more hydrophilic and open, facilitating the improvement in water permeability of the membrane.

Although different organosilica precursors have been applied in the development of molecular separation membranes in recent years, very little work has effectively elucidated the relationship between the microstructure and separation properties of these membranes, because most research has typically used only one type of organosilica membrane. The influences of size, flexibility, and shape of the organic bridges on material's properties were only recently reported using alkyl (CH_2, C_2H_4, and C_8H_{16}) and aromatic (benzene and biphenyl) bridges with different sizes.[15] In the present study, we offer a detailed examination of the microstructure-separation properties of organosilica membranes by using ethane, ethylene, and acetylene bridges of similar lengths. The only difference is the single versus double versus triple bond of each organic bridge, and this will provide new insights into the microstructure-separation properties of the organosilica membranes, which benefits the tailoring of the membrane structure and performances.

EXPERIMENTAL SECTION

Monomer Synthesis. 1,2-Bis(triethoxysilyl)acetylene (BTESA) was prepared in a fashion similar to that reported previously.[16] In a 500 mL three necked flask fitted with a reflux condenser was placed dry $(C_2H_5)_2O$ (200 mL) and 1.65 M n-C_4H_9Li (90 mL, 150 mmol). The mixture was cooled to −78 °C, and tetrachloroethene (4.5 mL, 50 mmol) dissolved in dry $(C_2H_5)_2O$ (15 mL) was slowly added to the mixture. Then, the mixture was stirred for 1 h at this temperature and further stirred for 12 h at room temperature to form white precipitates. The mixture was again cooled to −78 °C, and chlorotriethoxysilane (20 mL, 100 mmol) in $(C_2H_5)_2O$ (30 mL) was slowly added to the mixture, which was then warmed to room temperature and stirred for 12 h. The resultant LiCl precipitates were filtrated, and the solvents were evaporated. Distillation of the residue under reduced pressure (82 °C, 0.5 mmHg) gave BTESA monomer (7.2 g, 41% yield) as a colorless oil: ^1H NMR (δ in $CDCl_3$) 3.89 (q, 12H, J = 7.0 Hz), 1.26 (t, 18H, J = 7.0 Hz); ^{13}C NMR (δ in CDCl3) 103.94, 59.18, 17.98 (Figure 1); ^{29}Si NMR (δ in $CDCl_3$) −75.70; high-resolution ESI-MS m/z = 373.14694 $[M + Na]^+$ (calcd. for $C_{14}H_{30}O_6NaSi_2$: 373.14731).

Sol Synthesis. 1,2-Bis(triethoxysilyl)acetylene (BTESA) sol was synthesized via the hydrolysis and polymerization reaction of $(EtO)_3SiC{\equiv}CSi(OEt)_3$ with water and HCl, in ethanol. A required amount of BTESA was mixed with ethanol. Subsequently, premixed water and HCl were added dropwise to the precursor mixture under continuous stirring. The molar composition of the reactants was BTESA/H_2O/HCl = 1:60:0.1, and the weight percent of BTESA was kept at 5.0 wt %. The solution was stirred for 2 h at 25 °C before coating. 1,2-Bis(triethoxysilyl)ethane (BTESE, Gelest, Inc.) and 1,2-bis(triethoxysilyl)ethylene (BTESEthy, ∼80% trans isomer, Gelest, Inc.) sols were prepared under the same conditions as the BTESA sol.

Membrane Preparation. Tubular α-alumina microfiltration membranes (porosity, 50%; average pore size, 1 μm; outside diameter, 10 mm; length, 100 mm) were used as the supports. First, α-alumina powders (average particle size were 0.2 and 1.9 μm, respectively) were coated onto the outer surface of the support using silica-zirconia colloidal sols as a binder, and the support was fired at 550 °C for 30 min. This coating and firing process was repeated several times to remove large pores that might have resulted in pinholes in the membrane. Then, SiO_2−ZrO_2 (molar ratio of Si/Zr = 1/1) colloidal sols were coated onto the substrate and fired at 550 °C to form an intermediate layer. Finally, the organosilica sol was deposited onto the intermediate layer by wipe coating using a wet cloth with the sol (0.5 wt %), followed by calcination at 300 °C in air for 20 min.

Characterization. The size distribution of the sols was measured by dynamic light scattering (DLS) using a Malvern Zetasizer Nano-ZS (ZEN3600). Thermogravimetric (TG) analysis (DTG-60, Shimadzu) was conducted on the organosilica powder to evaluate the decomposition behavior of the remaining organic components in air and N_2, respectively, with a heating rate of 10 °C min^{-1}. A Fourier transform infrared spectrometer (FT/IR-4100, JASCO) was applied to confirm the chemical structure of films. Films for FTIR and static contact angle measurements were obtained by coating the organosilica sols onto clean silicon wafers, followed by calcination at 300 °C for 20 min.

The microstructures and surface properties of the membranes were examined by nitrogen sorption at 77 K, using a Belsorp-Max (Bel

Japan, Inc.) instrument. Before analysis, the samples were outgassed at 200 °C overnight under vacuum. The Brunauer–Emmett–Teller (BET) method in a relative pressure range of P/P_0 = 0.01–0.25 was employed to calculate the specific surface area. The micropore volume was estimated using the *t*-plot method.

Positron annihilation lifetime (PAL) measurements, which enable quantitative evaluation of sub-nanoscale pores that N_2 molecules cannot access, were performed for the prepared powders. A ^{22}Na positron source of 0.7 MBq was sandwiched by the sample powders and a measurement system was equipped with a calibrated digital oscilloscope. The PAL data were recorded by accumulating annihilation events above 1 million count through determining time intervals between the start signal due to the emission of a characteristic γ ray at a β^+ decay of ^{22}Na and the corresponding stop signal due to the positron annihilation γ ray. The average positron lifetimes for the present samples were calculated by fitting the PAL data to the convolution of a model function *C* for the positron annihilations with a time resolution function *R* of the measurement system expressed as follows:

$$f(T) = A\int_{-\infty}^{\infty} R(t)\,\Theta(T-t)\,C(T-t)\,\mathrm{d}t + B \tag{1}$$

where *A*, *B*, and Θ are the normalized factor, background, and Heaviside-step function, respectively. *C* as a function of time *T*, consisting of several decay components is expressed by

$$C(T) = \sum_{i=1}^{n} \frac{I_i}{\tau_i}\exp\left(-\frac{T}{\tau_i}\right) \tag{2}$$

where τ, *I*, and *n* represent the average lifetime, relative intensity for each annihilation component, and the number of the decay components, respectively. $R(t)$ was approximated by a Gaussian function,

$$R(t) = \exp\left(-\frac{(t-a)^2}{b^2}4\log 2\right) \tag{3}$$

where *a* and b^2 are the shift factor and the Gaussian distribution, respectively. The full width at half-maximum of $R(t)$ was estimated to be about 170 ps for the present measurement system. In the analysis, five components were assumed for the positron lifetimes, providing the optimum fitting result.

The decay components of the PAL data were ascribed to the annihilations of free positron and positronium Ps, the positron-electron bound state existing either as spin-antiparallel *para*-positronium *p*-Ps or spin-parallel *ortho*-positronium *o*-Ps. The average lifetimes longer than 1 ns due to the *o*-Ps annihilation in pores were determined to be τ_3, τ_4, and τ_5 with relative intensities of I_3, I_4, and I_5, while the shorter lifetime components of τ_1 and τ_2 due to the annihilations of *p*-Ps and free positrons were found to be approximately 130 ns ($I_1 \sim 10\%$) and 440 ns ($I_2 \sim 60\%$), respectively. A pore radius, r_{Ps} [nm], smaller than 1.0 nm was estimated from τ_{Ps} [ns] for *o*-Ps having an average lifetime shorter than 20 ns based on a simple semiempirical quantum-mechanical model[17] as follows:

$$\tau_{Ps} = 0.5\left[1 - \frac{r_{Ps}}{r_{Ps}+0.166} + \frac{1}{2\pi}\sin\left(\frac{2\pi r_{Ps}}{r_{Ps}+0.166}\right)\right]^{-1} \tag{4}$$

Membrane Performance. Single gas permeation measurements were performed at 200 °C using high-purity He, H_2, CO_2, N_2, C_3H_6, C_3H_8, and SF_6. Prior to measurement, the membrane was dried for 8–10 h in a He flow of 20 mL/min at 200 °C to remove the adsorbed water from the membrane pores. The permeate stream was kept at atmospheric pressure, and the pressure drop across the membrane was maintained at 1 bar. The permeation rate was measured using a soap-film flow meter.

Desalination experiments were carried out using 2000 ppm of NaCl aqueous solution at 25 °C, and molecular weight cutoff (MWCO) measurements were performed using 500 ppm neutral solutes: ethanol, isopropanol, glucose, and sucrose. RO experiments were conducted using a typical RO testing apparatus as previously described.[18] The feed solution, pressurized at 1.15 MPa with a plunger pump, was vigorously agitated in the RO cell, and the retentate was recycled at an approximate flow of 30 mL min^{-1}. Water permeability, L_p, was calculated from the volume flux, J_v, divided by the effective transmembrane pressure, $\Delta P - \Delta\pi$.

$$J_v = L_p(\Delta P - \Delta\pi) \tag{5}$$

where L_p is the water permeability and, ΔP ($=P_1 - P_2$) and $\Delta\pi$ ($=\pi_1 - \pi_2$) are the differences in applied pressure and osmotic pressure, respectively. Osmotic pressure was calculated as an ideal solution. The observed rejection, R_{obs}, can be expressed as follows:

$$R_{obs} = (1 - C_p/C_f) \times 100\% \tag{6}$$

The concentrations of feed (C_f) and permeate (C_p) were measured using a conductivity meter for NaCl and a total organic carbon analyzer (TOC-V_E, Shimadzu) for neutral solutes. Each test was first run for at least 3 h to confirm a steady state, and then the permeate sample was collected and analyzed. Each experimental data point shown in this study is the average value of 3 samples. The variations in the data for gas permeance, water permeability, and observed rejection during each measurement were less than 4%, 5%, and 2%, respectively.

RESULTS AND DISCUSSION

Size distributions of the BTESE, BTESEthy, and BTESA sols with an alkoxide concentration of 0.3 mol L^{-1} were determined by dynamic light scattering at 25 °C, as presented in Figure 2.

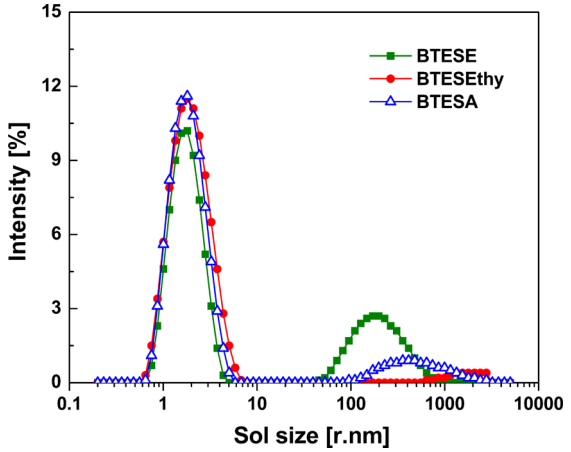

Figure 2. Size distribution of the BTESE, BTESEthy, and BTESEthy sols, as determined by DLS.

Freshly synthesized (~2h for hydrolysis and polymerization reaction) BTESE sol showed a bimodal size distribution with a mean radius of 4.7 nm, likely due to a small fraction of polymerization reaction of the monomer species.[19] In contrast, a narrow size distribution was observed for freshly prepared BTESEthy and BTESA sols, with a mean radius of 1.9 and 2.1 nm, respectively. In general, the small sol size and narrow size distribution was desirable for the preparation of a thin, microporous separation layer.[15] It should be noted that the sols needed for membrane fabrication were filtered (filter size, 0.1 μm) to minimize the effect of larger sols.

Thermogravimetric (TG) analysis was conducted to evaluate the thermal stability of the organically bridged silica network. TG measurement was initiated after drying the sample at 100 °C for 2 h under a flow of either air or N_2. As shown in Figure 3 (left), the weight losses of a BTESA-derived gel powder under air and N_2 atmospheres at 800 °C were 17.4% and 13.6%,

dx.doi.org/10.1021/am501731d | ACS Appl. Mater. Interfaces 2014, 6, 9357–9364

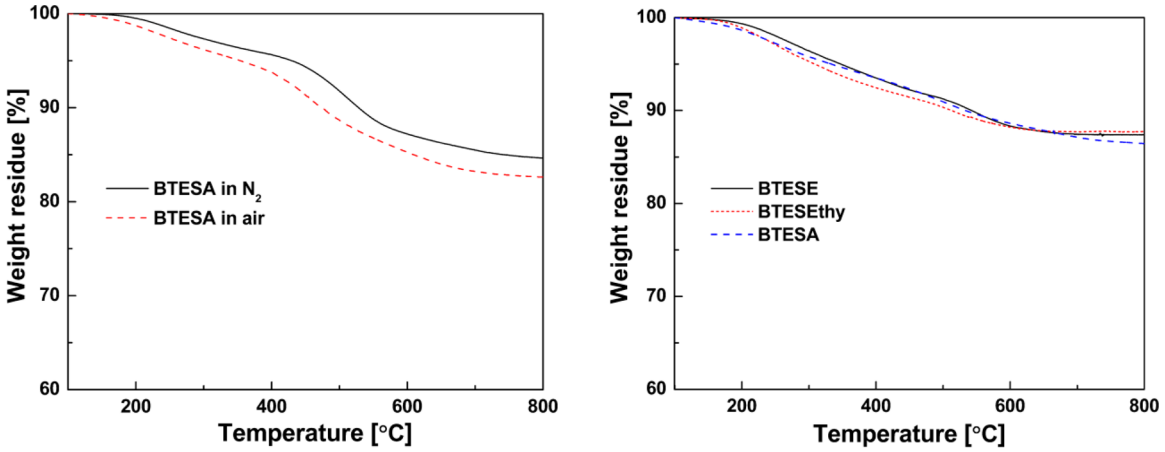

Figure 3. (left) TG analysis of BTESA gels under air and N_2 atmospheres with a heating rate of 10 °C/min, and (right) comparison of TG curves of BTESE, BTESEthy, and BTESA gels under a N_2 atmosphere.

respectively. TG weight residue decreased gradually at 200–400 °C probably due to the evaporation of adsorbed water and to the dehydration of the silanol groups. Another decrease in weight was observed above approximately 400 °C, and was more pronounced in air than in N_2, which suggests the decomposition of acetylene groups in the network.[20] Figure 3 (right) shows TG curves of BTESE, BTESEthy, and BTESA gels under a N_2 atmosphere. There was no significant difference in the weight loss among the three materials. Therefore, organosilica membranes derived from BTESE, BTESEthy, and BTESA were expected to be thermally stable at least up to 300 °C.

Figure 4 shows the FTIR spectra of the BTESE, BTESEthy, and BTESA films. The following absorptions were mainly

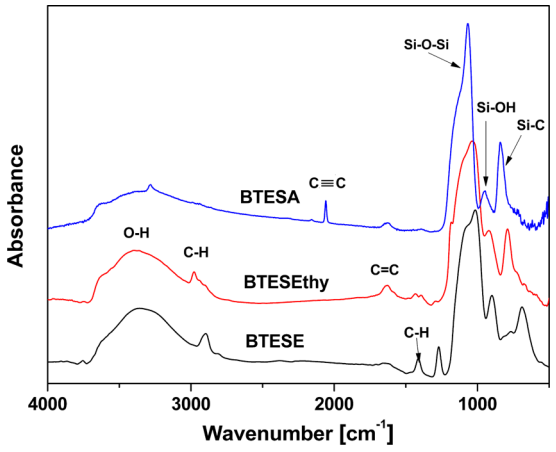

Figure 4. FTIR spectra of BTESE, BTESEthy, and BTESA films fired at 300 °C in air.

related to the structure of the organosilica networks: C=C stretch (~1640 cm^{-1}); C≡C (~2100 cm^{-1}); O–H stretch (~3000–3600 cm^{-1}); C–H vibrations at ~1410 cm^{-1} (CH_2 bend), ~2890 cm^{-1} (CH_2 stretch), ~2980 cm^{-1} (=CH stretch); Si–O–Si stretch (1020–1200 cm^{-1}); Si–OH stretch (~920 cm^{-1}); and Si–C stretch (~790 cm^{-1}).[21−23] The presence of these characteristic bands verified the formation of the related organosilica networks. However, compared to the BTESE film, the BTESEthy and BTESA samples showed shifted absorptions in the region of Si–C and C–H stretching vibrations. For example, the characteristic peaks of Si–C stretch appeared at 710, 780, and 820 cm^{-1} in the BTESE, BTESEthy, and BTESA samples, respectively. Obviously, the peaks were shifted to higher wavenumbers with increasing bond strength.

Single gas permeance was measured using He, H_2, CO_2, N_2, C_3H_6, C_3H_8, and SF_6 for the three membranes with different bridging groups, as shown in Figure 5. The H_2 permeance and

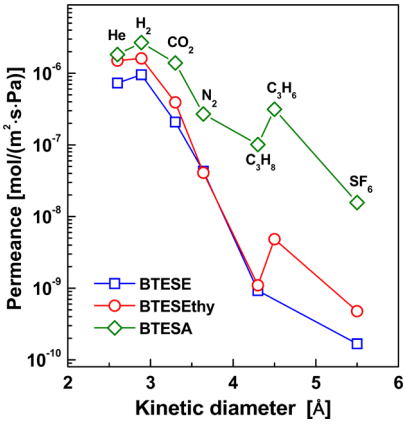

Figure 5. Comparison of gas permeance properties for BTESE, BTESEthy, and BTESA membranes at 200 °C.

relevant permeance ratios of H_2/N_2 and H_2/SF_6 are listed in Table 1. On the whole, the BTESA membrane exhibited higher

Table 1. H_2 Permeance (P_{H2}) and Permeance Ratios of H_2/N_2 and H_2/SF_6 at 200 °C

membrane	P_{H2} (mol/m² s Pa)	H_2/N_2	H_2/SF_6
BTESE	0.95×10^{-6}	22.2	5700
BTESEthy	1.61×10^{-6}	39.5	2590
BTESA	2.68×10^{-6}	10.3	789

permeance with the lowest permeance ratios for H_2/N_2 and H_2/SF_6, suggesting a relatively loose structure. In contrast, higher permeance ratios for H_2/N_2 and H_2/SF_6 were observed for BTESE and BTESEthy membranes, indicating their superior molecular sieving ability. Additionally, the $\pi-\pi$ interaction between unsaturated bridging groups and the C_3H_6 molecules may have contributed to the preferential permeation of C_3H_6

dx.doi.org/10.1021/am501731d | ACS Appl. Mater. Interfaces 2014, 6, 9357–9364

through the BTESEthy and BTESA membranes, considering that the molecular sizes of C_3H_6 and C_3H_8 are quite close.[24]

To further probe the microstructures, N_2 sorption and positron annihilation lifetime (PAL) measurements were performed on the BTESE, BTESEthy, and BTESA samples. All N_2 isotherms showed type-I characteristics, and no hysteresis was observed (Figure 6), which is typical of

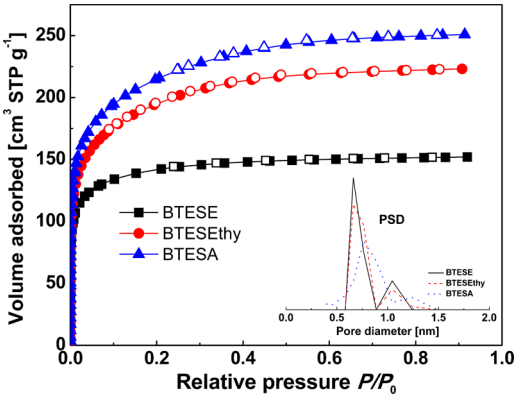

Figure 6. N_2 adsorption/desorption isotherms and pore size distributions (inset, PSD) of BTESE, BTESEthy, and BTESA samples.

microporous materials. However, the BTESA sample showed a wider pore size distribution in the microporous region, compared with BTESE and BTESEthy (Figure 6, inset). Details of the textural properties are given in Table 3. It is interesting to note that, from BTESE to BTESA, the micropore volume increased gradually together with an apparent increase in the BET specific surface area. This can be ascribed to the changes in the microstructure in these materials. The rigidity of the organic bridges increased from BTESE to BTESA. The organosilica networks with larger rigid bridges would further prevent the collapse of pores and the formation of dead-end pores during the calcination process, hence affording a more open and accessible pore structure.[25,26]

Figure 7 shows the PAL data for the present powders. All data clearly display the long-lived *o*-Ps component in a range of longer than 1 ns due to the annihilation of the positrons in the pores. The analyzed average lifetimes, τ_{Ps}, for the *o*-Ps components are listed in Table 2 with their relative intensities, I_{Ps}. As seen in the table, the BTESE and BTESEthy powders had a lifetime component longer than 20 ns in addition to those between 1 and 20 ns, while BTESA did not. The longest lifetimes $\tau_{Ps\text{-}3}$ (>20 ns) suggested that the former two powders had both micropores and mesopores,[27] whereas BTESA had only micropores. This was probably due to the relatively broad pore size distribution of BTESE and BTESEthy networks compared with BTESA networks. From τ_{Ps} shorter than 20 ns, the average radii, r_{Ps}, were calculated based on eq 4, particularly focusing on micropores. As a result, the obtained r_{Ps} ranged from 0.18 to 0.56 nm (BTESE and BTESEthy), and from 0.13 to 0.63 nm (BTESA) (Table 3). By considering the effective size of gas molecules, the pore size from the first component for BTESA ($r_{Ps\text{-}1}$ = 0.13 nm) was obviously not associated with the gas permeance. In light of this interpretation, the mean radii $\tilde{r} = \Sigma r_{Ps} I_{Ps} / \Sigma I_{Ps}$ for the micropores, involved with the molecular transport of interest, were expected to be 0.41 and 0.53 nm for the former two powders and BTESA, respectively.

The effective pore sizes of the BTESA membranes were evaluated by measuring the MWCO using a series of neutral

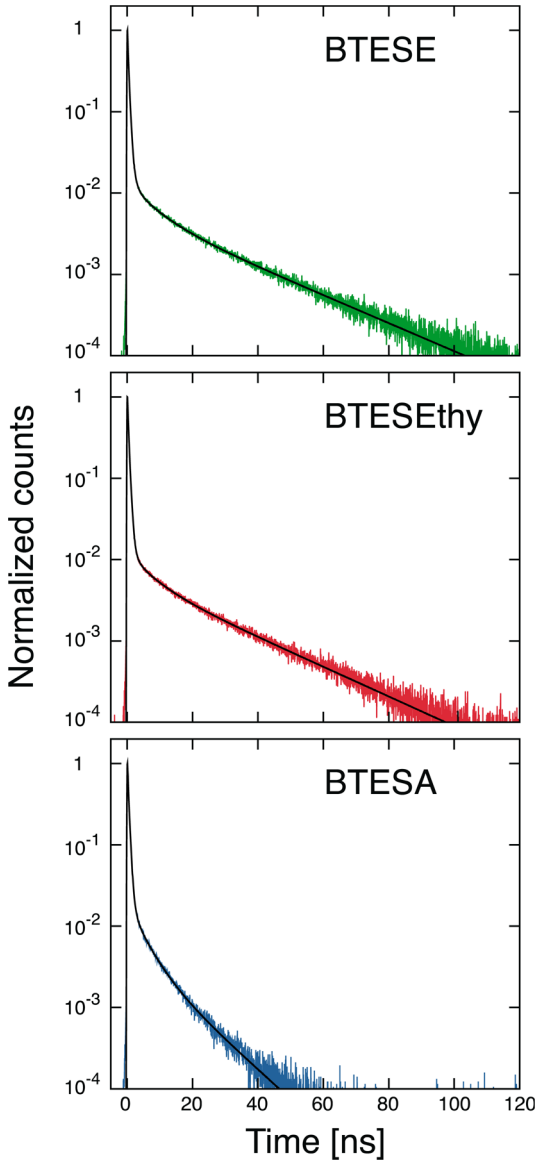

Figure 7. PAL data (corrected for the background) for the BTESE, BTESEthy, and BTESA powders. The solid lines represent fitting curves to the respective data.

Table 2. Average Lifetimes τ_{Ps} and Relative Intensities I_{Ps} of *ortho*-Positronium *o*-Ps for the BTESE, BTESEthy, and BTESA Powders[a]

sample	$\tau_{Ps\text{-}1}$ [ns]	$I_{Ps\text{-}1}$ [%]	$\tau_{Ps\text{-}2}$ [ns]	$I_{Ps\text{-}2}$ [%]	$\tau_{Ps\text{-}3}$ [ns]	$I_{Ps\text{-}3}$ [%]
BTESE	1.24	14.2	7.16	21.9	20.2	64.0
BTESEthy	1.19	9.9	6.44	19.6	23.8	70.5
BTESA	1.03	18.2	4.31	42.3	12.0	39.5

[a] I_{Ps} is normalized to the overall intensity of the *o*-Ps components.

Table 3. Textural Properties and Average Radii r_{Ps} of the Micropores for the BTESE, BTESEthy, and BTESA Samples

sample	S_{BET} (m^2/g)	V_p (cm^3/g)	$r_{Ps\text{-}1}$ [nm]	$r_{Ps\text{-}2}$ [nm]	$r_{Ps\text{-}3}$ [nm]
BTESE	522	0.25	0.19	0.56	N/A
BTESEthy	661	0.33	0.18	0.54	N/A
BTESA	763	0.40	0.13	0.44	0.63

dx.doi.org/10.1021/am501731d | ACS Appl. Mater. Interfaces 2014, 6, 9357−9364

solutes with different sizes: isopropanol (Stokes diameter (Sd): 0.48 nm), glucose (Sd: 0.73 nm), and sucrose (Sd: 0.94 nm).[28,29] Figure 8 shows the MWCO curves of the BTESA membrane and a comparison with the BTESE and BTESEthy membrane, together with the commercial polyamide RO membrane, SW30HR. The MWCO, defined at 90% rejection, of the BTESA membrane was approximately 100 Da, which was distinctly larger than that of ~50 Da for BTESE and BTESEthy membranes, and similar to that of SW30HR.[30] This result clearly indicated that a larger effective pore size was obtained by the introduction of acetylene bridges in the organosilica network, which is quite consistent with gas permeation results. In addition, the incomplete rejection of glucose and sucrose suggested the presence of a small fraction of large pores in the membrane, probably derived from the pore size distribution of amorphous silica networks.

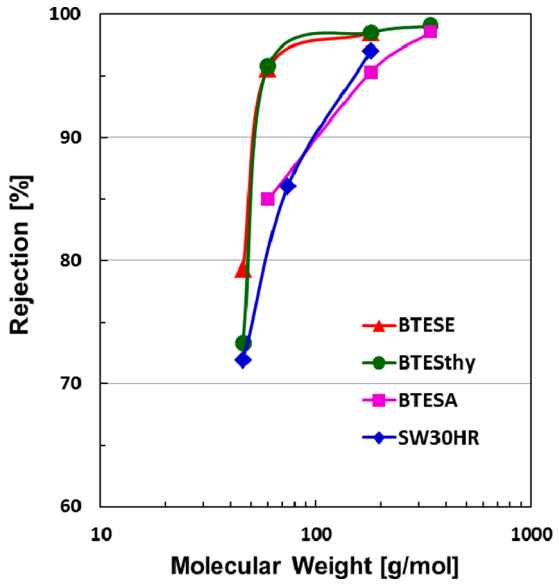

Figure 8. Comparison of molecular weight cutoff for the BTESE, BTESEthy, and BTESA membranes with the commercial polyamide RO membrane, SW30HR (Dow FilmTec).

Figure 9 shows the trade-off relationship between NaCl rejection and water permeability for the three types of organosilica RO membranes. Even at a low pressure of 1.15 MPa, the BTESE and BTESEthy membranes almost completely (>97%) rejected NaCl. Despite a relatively low NaCl rejection of ~95%, the water permeability of the BTESA membranes reached 8.5×10^{-13} $m^3/(m^2 \cdot s \cdot Pa)$, which was about 8 times higher than that of the BTESE membrane. The high water permeability can be attributed to the incorporation of polarizable and rigid acetylene bridges in the networks, which makes the membrane network more hydrophilic and open. Table 4 shows the water contact angles of the BTESE, BTESEthy, and BTESA films. BTESEthy and BTESA films with unsaturated bridges showed low contact angles, suggesting their higher surface hydrophilicity. More importantly, a uniform distribution of bridging groups led to the increased hydrophilicity not only on the membrane surface but also inside the membrane (within the pore channels of the network).[31,32] This increased hydrophilicity on both the inside and the surface may play a leading role in the improved water permeability.

To elucidate the microstructure and electron density distributions of the BTESE, BTESEthy, and BTESA networks,

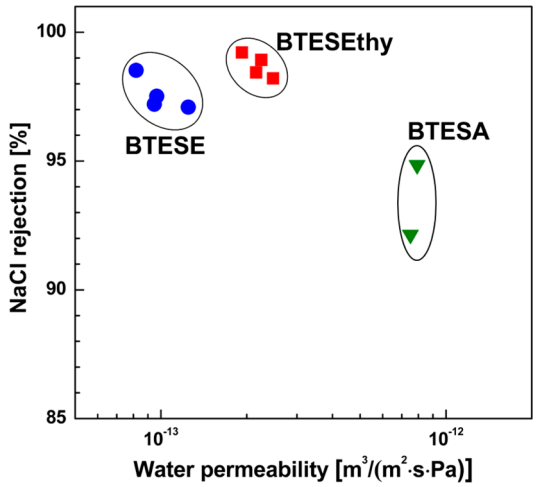

Figure 9. Trade-off of water permeability versus salt rejection for the organosilica RO membranes (25 °C, 1.15 MPa, and 2000 ppm of NaCl).

Table 4. Contact Angles (CA) of BTESE, BTESEthy, and BTESA films

sample	CA (deg)
BTESE	66.8 ± 1.4
BTESEthy	50.4 ± 2.1
BTESA	48.4 ± 1.3

quantum chemical calculations were carried out. As shown in Figure 10, model molecules with a trimeric 15-membered ring structure were employed for the calculations, because these seemed to be the smallest strain-free systems among the cyclic oligomers. The siloxy linkages on the silicon atoms in the real systems were replaced by methoxy groups in the models for simplification to minimize the computation time. The geometries were optimized by semiempirical calculations using the PM6 set of parameters and the electrostatic potentials (ESPs) were computed using the optimized geometries at B3LYP/6-31G(d) level of theory. The optimized geometries showed that the inner ring through space C···C distance increased gradually from BTESE to BTESA, suggesting an increasingly more open pore structure of the models, probably due to increased rigidity in the network. In addition, C−H bonds located in the pores of BTESE and BTESEthy appeared to hinder the molecules passing through the pores. The electrostatic potentials (ESPs) of the three models showed that the negative potentials were mainly localized inside the rings. However, the BTESA and BTESEthy models exhibited a higher contrast for positive and negative potentials, compared with the BTESE model, which led to an enhanced H_2O-affinity for the channels by hydrogen-bonding and/or dipole−dipole interaction.

CONCLUSIONS

We developed ethane-, ethylene-, and acetylene-bridged organosilica membranes and presented a detailed examination of the microstructure-separation properties of these organosilica membranes. Small sol size with narrow size distribution was obtained for the BTESA sol by optimizing the synthesis procedures. Gas permeation measurements indicated that a looser structure was obtained by introducing larger rigid acetylene bridges in the network. N_2 sorption and positron annihilation lifetime (PAL) were applied to further quantita-

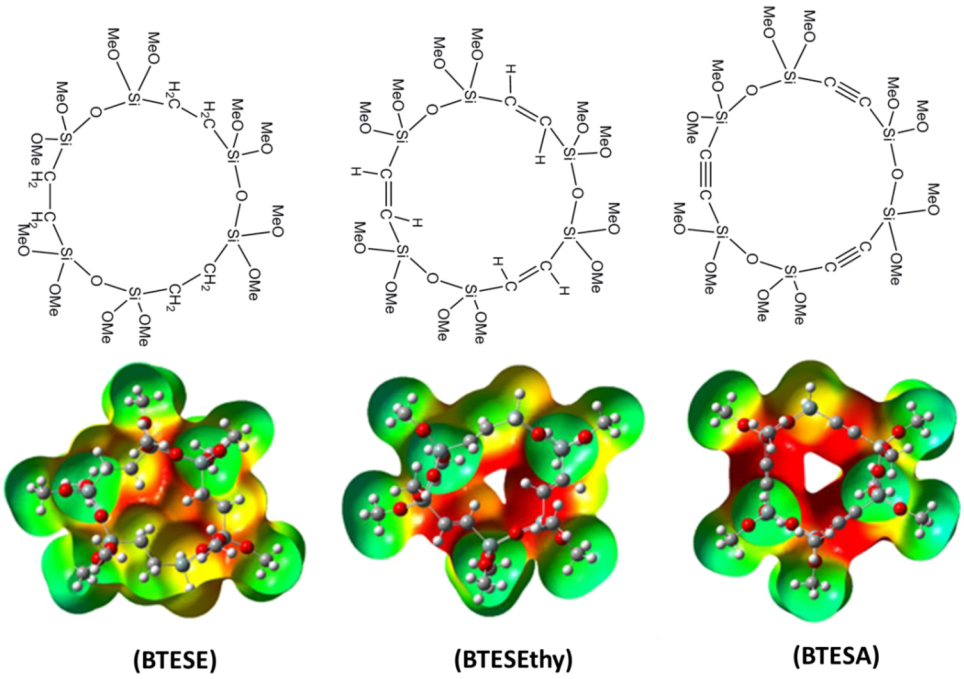

Figure 10. Optimized structures and ESPs for models of (left) BTESE, (middle) BTESEthy, and (right) BTESA networks derived from quantum chemical simulations at PM6//B3LYP/6-31G(d). Colors range from red to green denoting extremely electron-rich and -deficient regions, respectively.

tively evaluate the microstructures of organosilica networks. In MWCO measurements, BTESA membranes exhibited a larger effective separation pore size than BTESE and BTESEthy membranes, resulting in a relatively low NaCl rejection in RO desalination. The water permeability of the BTESA membranes reached approximately 8.5×10^{-13} $m^3/(m^2 \cdot s \cdot Pa)$ due to the enhanced H_2O-affinity both in the pore channels and on the membrane surface. In quantum chemical calculations, the acetylene-bridged BTESA network showed more open pore structure and increased polarization, leading to the significant improvement in water permeability.

AUTHOR INFORMATION

Corresponding Author

*E-mail: tsuru@hiroshima-u.ac.jp.

Notes

The authors declare no competing financial interest.

ACKNOWLEDGMENTS

This research is supported by Core Research for Evolutional Science and Technology (CREST) Program of Japan Science and Technology Agency (JST).

REFERENCES

(1) Hoffmann, F.; Cornelius, M.; Morell, J.; Froeba, M. Silica-Based Mesoporous Organic-Inorganic Hybrid Materials. *Angew. Chem., Int. Ed.* **2006**, *45*, 3216−3251.

(2) Thomas, A. Functional Materials: From Hard to Soft Porous Frameworks. *Angew. Chem., Int. Ed.* **2010**, *49*, 8328−8344.

(3) Inagaki, S.; Guan, S.; Fukushima, Y.; Ohsuna, T.; Terasaki, O. Novel Mesoporous Materials with a Uniform Distribution of Organic Groups and Inorganic Oxide in Their Frameworks. *J. Am. Chem. Soc.* **1999**, *121*, 9611−9614.

(4) Asefa, T.; MacLachlan, M. J.; Coombs, N.; Ozin, G. A. Periodic Mesoporous Organosilicas with Organic Groups inside the Channel Walls. *Nature* **1999**, *402*, 867−871.

(5) Melde, B. J.; Holland, B. T.; Blanford, C. F.; Stein, A. Mesoporous Sieves with Unified Hybrid Inorganic/Organic Frameworks. *Chem. Mater.* **1999**, *11*, 3302−3308.

(6) Van Der Voort, P.; Esquivel, D.; De Canck, E.; Goethals, F.; Van Driessche, I.; Romero-Salguero, F. J. Periodic Mesoporous Organosilicas: from Simple to Complex Bridges; a Comprehensive Overview of Functions, Morphologies and Applications. *Chem. Soc. Rev.* **2013**, *42*, 3913−3955.

(7) Hatton, B.; Landskron, K.; Whitnall, W.; Perovic, D.; Ozin, G. A. Past, Present, and Future of Periodic Mesoporous Organosilicas-The PMOs. *Acc. Chem. Res.* **2005**, *38*, 305−312.

(8) Castricum, H. L.; Sah, A.; Kreiter, R.; Blank, D. H. A.; Vente, J. F.; ten Elshof, J. E. Hybrid Ceramic Nanosieves: Stabilizing Nanopores with Organic Links. *Chem. Commun.* **2008**, 1103−1105.

(9) Castricum, H. L.; Sah, A.; Kreiter, R.; Blank, D. H. A.; Vente, J. F.; ten Elshof, J. E. Hydrothermally Stable Molecular Separation Membranes from Organically Linked Silica. *J. Mater. Chem.* **2008**, *18*, 2150−2158.

(10) Kanezashi, M.; Yada, K.; Yoshioka, T.; Tsuru, T. Design of Silica Networks for Development of Highly Permeable Hydrogen Separation Membranes with Hydrothermal Stability. *J. Am. Chem. Soc.* **2009**, *131*, 414−415.

(11) Qi, H.; Han, J.; Xu, N. P.; Bouwmeester, H. J. M. Hybrid Organic-Inorganic Microporous Membranes with High Hydrothermal Stability for the Separation of Carbon Dioxide. *ChemSusChem* **2010**, *3*, 1375−1378.

(12) Xu, R.; Wang, J. H.; Kanezashi, M.; Yoshioka, T.; Tsuru, T. Development of Robust Organosilica Membranes for Reverse Osmosis. *Langmuir* **2011**, *27*, 13996−13999.

(13) Chua, Y. T.; Lin, C. X. C.; Kleitz, F.; Zhao, X. S.; Smart, S. Nanoporous Organosilica Membrane for Water Desalination. *Chem. Commun.* **2013**, *49*, 4534−4536.

(14) Xu, R.; Kanezashi, M.; Yoshioka, T.; Okuda, T.; Ohshita, J.; Tsuru, T. Tailoring the Affinity of Organosilica Membranes by Introducing Polarizable Ethenylene Bridges and Aqueous Ozone Modification. *ACS Appl. Mater. Interfaces* **2013**, *5*, 6147−6154.

(15) Castricum, H. L.; Paradis, G. G.; Mittelmeijer-Hazeleger, M. C.; Kreiter, R.; Vente, J. F.; ten Elshof, J. E. Tailoring the Separation Behavior of Hybrid Organosilica Membranes by Adjusting the

Structure of the Organic Bridging Group. *Adv. Funct. Mater.* **2011**, *21*, 2319−2329.
(16) Shea, K. J.; Loy, D. A.; Webster, O. Arylsilsesquioxane Gels and Related Materials. New Hybrids of Organic and Inorganic Networks. *J. Am. Chem. Soc.* **1992**, *114*, 6700−6710.
(17) Eldrup, M.; Lightbody, D.; Sherwood, J. N. The Temperature Dependence of Positron Lifetimes in Solid Pivalic Acid. *Chem. Phys.* **1981**, *63*, 51−58.
(18) Xu, R.; Wang, J. H.; Kanezashi, M.; Yoshioka, T.; Tsuru, T. Reverse Osmosis Performance of Organosilica Membranes and Comparison with the Pervaporation and Gas Permeation Properties. *AIChE J.* **2013**, *59*, 1298−1307.
(19) Tobler, D. J.; Shaw, S.; Benning, L. G. Quantification of Initial Steps of Nucleation and Growth of Silica Nanoparticles: An In-situ SAXS and DLS Study. *Geochim. Cosmochim. Acta* **2009**, *73*, 5377−5393.
(20) Tsuru, T.; Nakasuji, T.; Oka, M.; Kanezashi, M.; Yoshioka, T. Preparation of Hydrophobic Nanoporous Methylated SiO_2 Membranes and Application to Nanofiltration of Hexane Solutions. *J. Membr. Sci.* **2011**, *384*, 149−156.
(21) Ngamou, P. H. T.; Overbeek, J. P.; Kreiter, R.; van Veen, H. M.; Vente, J. F.; Wienk, I. M.; Cuperus, P. F.; Creatore, M. Plasma-Deposited Hybrid Silica Membranes with a Controlled Retention of Organic Bridges. *J. Mater. Chem. A* **2013**, *1*, 5567−5576.
(22) Esquivel, D.; De Canck, E.; Jimenez-Sanchidrian, C.; Van Der Voort, P.; Romero-Salguero, F. J. Formation and Functionalization of Surface Diels-Alder Adducts on Ethenylene-Bridged Periodic Mesoporous Organosilica. *J. Mater. Chem.* **2011**, *21*, 10990−10998.
(23) Schmeltzer, J. M.; Porter, L. A.; Stewart, M. P.; Buriak, J. M. Hydride Abstraction Initiated Hydrosilylation of Terminal Alkenes and Alkynes on Porous Silicon. *Langmuir* **2002**, *18*, 2971−2974.
(24) Kanezashi, M.; Kawano, M.; Yoshioka, T.; Tsuru, T. Organic-Inorganic Hybrid Silica Membranes with Controlled Silica Network Size for Propylene/Propane Separation. *Ind. Eng. Chem. Res.* **2012**, *51*, 944−953.
(25) Loy, D. A.; Carpenter, J. P.; Yamanaka, S. A.; McClain, M. D.; Greaves, J.; Hobson, S.; Shea, K. Polymerization of Bis(triethoxysilyl)-ethenes. Impact of Substitution Geometry on the Formation of Ethenyleneand Vinylidene-Bridged Polysilsesquioxanes. *J. Chem. Mater.* **1998**, *10*, 4129−4140.
(26) Shea, K. J.; Loy, D. A. Molecular-Engineered Hybrid Organic-Inorganic Materials. *Chem. Mater.* **2001**, *13*, 3306−3319.
(27) Ito, K.; Nakanishi, H.; Ujihira, Y. Extension of the Equation for the Annihilation Lifetime of ortho-Positronium at a Cavity Larger than 1 nm in Radius. *J. Phys. Chem. B* **1999**, *103*, 4555−4558.
(28) Wang, X. L.; Tsuru, T.; Nakao, S.; Kimura, S. The Electrostatic and Steric-Hindrance Model for the Transport of Charged Solutes through Nanofiltration Membranes. *J. Membr. Sci.* **1997**, *135*, 19−32.
(29) Kiso, Y.; Muroshige, K.; Oguchi, T.; Hirose, M.; Ohara, T.; Shintani, T. Pore Radius Estimation Based on Organic Solute Molecular Shape and Effects of Pressure on Pore Radius for a Reverse Osmosis Membrane. *J. Membr. Sci.* **2011**, *369*, 290−298.
(30) Hatakeyama, E. S.; Gabriel, C. J.; Wiesenauer, B. R.; Lohr, J. L.; Zhou, M. J.; Noble, R. D.; Gin, D. L. Water Filtration Performance of a Lyotropic Liquid Crystal Polymer Membrane with Uniform, Sub-1-nm Pores. *J. Membr. Sci.* **2011**, *366*, 62−72.
(31) Xia, Y. D.; Wang, W. X.; Mokaya, R. Bifunctional Hybrid Mesoporous Organoaluminosilicates with Molecularly Ordered Ethylene Groups. *J. Am. Chem. Soc.* **2005**, *127*, 790−798.
(32) Vercaemst, C.; Ide, M.; Wiper, P. V.; Jones, J. T. A.; Khimyak, Y. Z.; Verpoort, F.; Van Der Voort, P. Ethenylene-Bridged Periodic Mesoporous Organosilicas: From E to Z. *Chem. Mater.* **2009**, *21*, 5792−5800.